Synthesis and photoluminescence of Eu^{3+}-doped $LiZnVO_4$ nanopowders

M. H. HUANG, T. H. FANG[*], Y. C. FAN, M. H. LIN
Department of Mechanical Engineering, National Kaohsiung University of Science and Technology, Kaohsiung 807, Taiwan

The optical and structural properties of europium-doped lithium zinc vanadium oxide ($LiZnVO_4$:xEu) nanopowders, synthesized via a solid-state reaction, were studied. X-ray diffraction indicates that a rhombohedral $LiZnVO_4$ phase began to appear when annealing at 500ºC. The bandgap energy of pure and Eu^{3+}-doped $LiZnVO_4$ was around 3.20 and 3.22 eV, respectively. The photoluminescence spectra of pure $LiZnVO_4$ exhibit a strong emission peak at 526 nm when annealed at 600ºC. For the Eu^{3+}-doped $LiZnVO_4$ samples, the new emission peaks appear at 618 nm as the concentration of Eu^{3+} ions increases. The intensity of the emission peaks at 618 nm increases due to the $^5D_0 \rightarrow {}^7F_2$ transition. The CIE (Commission International de l'Éclairage) color coordinates of $LiZnVO_4$:xEu^{3+} (x = 0 mol%, 1 mol%, 3 mol%, 5 mol%, and 7 mol%) change from x = 0.262 and y = 0.457 to x = 0.264 and y = 0.437.

1. Introduction

Recently, oxide phosphor materials have been intensely studied mainly because of their higher chemical stability compared to sulfide phosphors [1-7]. Vanadium oxide materials have attracted a lot of attention due to their unique structure and optical and magnetic properties [1,5-7]. Vanadate compounds, such as $LiZnVO_4$, are widely found in electrochemical devices and sensors [5-10]. In addition, efficient optical materials doped with rare-earth ions are useful for various applications, e.g., display screens, light sources, and photonics devices [1,9,11-13]. Eu^{3+} ions are known to act as an activator center for luminescence phenomena [14]. Recently, Eu^{3+} materials have been actively studied because of the intra-4f-shell transitions from the excited energy level to the lower energy level $^5D_0 \rightarrow {}^7F_j$ (j = 1, 2, 3, 4) [15-18]. Because the emission of Eu^{3+} doped materials is mainly at 610–630 nm, red light emission is observed in various glasses and crystals [19-26].

Synthetic $LiZnVO_4$ is an interesting material for oxide phosphors because its components are not as environmentally polluting as other compounds [27]. $LiZnVO_4$ materials are widely used in rechargeable Li-ion batteries, resonators, and humidity sensors. Lin et al. [28] used $LiZnVO_4$ particles as anode material in a rechargeable Li-ion battery; the electrochemical measurements showed that the anode possessed excellent cycling stability. Busuioc et al. [8] found that $LiZnVO_4$ had excellent microwave dielectric properties in a resonator, and several reports [7,29-32] showed that $LiZnVO_4$ materials had remarkable sensitivity toward humidity and are widely used with doped gas-sensing components.

Several techniques have been reported for the synthesis of $LiZnVO_4$, including the sol-gel method [8], solvothermal techniques [33], and solid-state reactions [34]. Thus, there are many preliminary studies to explore whether it is an efficient phosphor host for luminescent materials. The rapid Vibro-milling method has been widely used for the preparation of various nanopowders due to its simplicity, low cost, and speed [35,36].

In this work, a fluorescent Eu^{3+}-doped $LiZnVO_4$ powder was prepared through a rapid Vibro-milling method. The crystal microstructure was analyzed by X-ray diffraction. The luminescence characteristics of the material were investigated. Furthermore, the influence of doping Eu^{3+} on the morphology, optical properties, and structure was evaluated.

2. Experiments

A rapid Vibro-milling method was used to synthesize Eu^{3+}-doped $LiZnVO_4$ powder. The raw materials included lithium carbonate (Li_2CO_3, 99%), vanadium oxide (V_2O_5, 99.6%), zinc oxide (ZnO, 99.9%) and europium oxide (Eu_2O_3, 99.9%, powder) for doping. The different proportions of the powders were obtained through vibration-milled for 9 hours. Then, the mixture

was placed in a muffle furnace and the temperature was increased to 5ºC per minute. The powders were calcined at 400ºC, 500ºC, 600ºC, and 700ºC, and maintained at that temperature for 3 hours. They were then allowed to cool inside the furnace, and Eu^{3+}-doped $LiZnVO_4$ was obtained.

The $LiZnVO_4$ and Eu^{3+} crystalline phases were determined by X-ray diffraction (XRD, Bruker D2 Phaser) irradiating with Cu Kα radiation of a wavelength of 1.5419 Å in the range $10° \leq 2\theta \leq 70°$. The surface morphology and microstructure of the samples were evaluated via scanning electron microscopy (SEM, JSM-6330TF, JEOL). The excitation and emission spectra and the CIE color coordinate diagram (Commission International de l'Éclairage) were obtained using a photoluminescence (PL) spectrometer (Hitachi, F-4500). The absorption spectra were acquired by a UV-Vis spectrometer (Jasco, V-670).

3. Results and discussion

Fig. 1(a) shows the XRD patterns of pure $LiZnVO_4$ sintered at different calcining temperatures. A single $LiZnVO_4$ phase with a rhombohedral structure was observed above 500ºC (JCPDS card no. 38–1332). The crystallinity degree of the powder calcined at 600ºC was high. Fig. 1(b) presents the XRD patterns of $LiZnVO_4$ calcined at 600ºC with different Eu^{3+} content. The sample doped with 1 mol% Eu^{3+} shows a secondary $Eu(VO_4)$ phase with a tetragonal structure (JPCDS card no. 86–0995). No secondary phases were detected in the pure $LiZnVO_4$ sample. The $LiZnVO_4$ crystallinity decreases with increasing Eu^{3+} content, likely because of internal stress causing structural deformation [37].
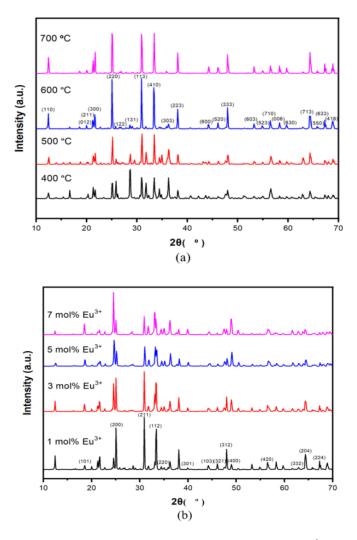

Fig. 1. (a) X-ray diffraction analysis of $LiZnVO_4$ at different annealed temperatures. (b) Eu^{3+}-doped $LiZnVO_4$ with increasing concentrations of Eu^{3+} annealed at 600ºC (color online)

The average grain size diameter can be calculated from the full width at half maximum (FWHM) of a peak by applying Scherrer's formula [38]:
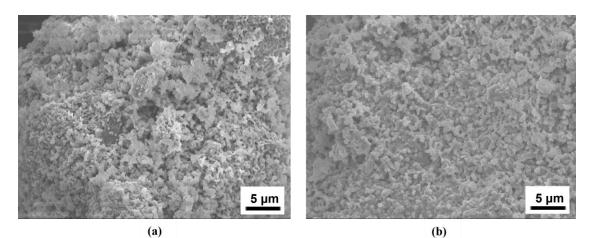
$$d = \frac{k\lambda}{\beta \cos\theta} \qquad (1)$$

where $k = 0.89$ represents the Scherrer constant, λ represents the X-ray wavelength (1.5419 Å), β represents half the peak width, and θ represents the position of the peak [38].

The grain sizes of crystalline pure LiZnVO₄ annealed at 400ºC, 500ºC, 600ºC, and 700ºC are around 46.56, 48.53, 59.87, and 62.54 nm, respectively. When increasing the annealing temperature, the average size increased. LiZnVO₄ doped with 1 mol%, 3 mol%, 5 mol%, and 7 mol% Eu³⁺ annealed at 600ºC showed grain sizes of around 60.70, 57.67, 45.86, and 52.31 nm, respectively. The average size decreased with the dopant content up to 5 mol%, then at 7 mol%, the grain size increased again.

Figs. 2(a)–(d) display the SEM images of pure LiZnVO₄ calcined at 400ºC, 500ºC, 600ºC, and 700ºC. The morphology of LiZnVO₄ changed depending on the calcination temperature. In Figs. 2(a) and (b), the particles and sizes seem to be evenly distributed. The higher sintering temperatures yield larger grains; i.e., as the sintering temperature increases, the particle size also increases. High temperatures may increase the atomic mobility leading to fast grain growth. Accordingly, Fig. 2(c) shows that, when calcined at 600ºC, LiZnVO₄ particles are larger and there is more agglomeration than at lower temperatures. In Fig. 2(d), when the calcination temperature is 700ºC, the particle size significantly increases.
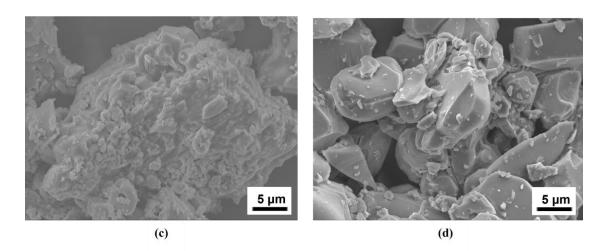

(a)

(b)

(c)

(d)

Fig. 2. SEM images of LiZnVO₄ phosphors synthesized at different annealed temperatures: (a) 400ºC, (b) 500ºC, (c) 600ºC, and (d) 700ºC

Figs. 3(a)–(d) correspond to the SEM images of LiZnVO₄ doped with 1, 3, 5, and 7 mol% Eu³⁺ annealed at 600ºC. The average size of the particles decreased with increasing Eu³⁺ concentration. Fig 3(a) shows that LiZnVO₄ doped with 1 mol% Eu³⁺ is very similar to pure LiZnVO₄ calcined at 600ºC, which presents agglomeration and large particles. Figs. 3(b)–(d) show the surface morphology of Eu³⁺-doped LiZnVO₄ is very similar.
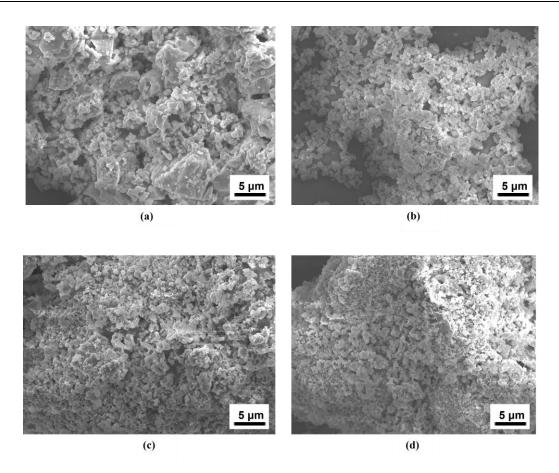
Fig. 3. SEM images of LiZnVO₄:xEu³⁺, (a) x = 1 mol%, (b) 3 mol%, (c) 5 mol%, and (d) 7 mol% annealed at 600ºC

Fig. 4 presents the absorption spectra of pure $LiZnVO_4$ and Eu^{3+}-doped $LiZnVO_4$ annealed at 600ºC. The 4f-4f transition absorption of Eu^{3+} is between 400 and 470 nm. The results of pure $LiZnVO_4$ are consistent with previous reports [39]. The additional absorption peaks at 467 and 536 nm are due to the transition from the $^7F_0$ ground state to the charge transfer state, i.e., the $^7F_0 \rightarrow {^5D_2}$ and $^7F_0 \rightarrow {^5D_1}$ transitions, respectively [16,37]. As the concentration of Eu^{3+} increased in the doped samples, the $^7F_0 \rightarrow {^5D_2}$ peak slightly shifted to shorter wavelengths (blue-shift).
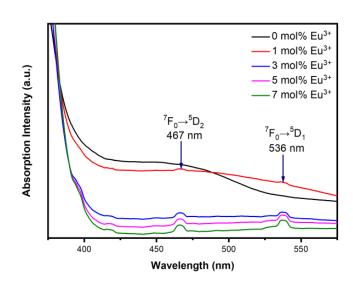

Fig. 4. Absorption spectra of pure LiZnVO₄, and LiZnVO₄:x Eu³⁺ (x = 0 mol%, 1 mol%, 3 mol%, 5 mol%, and 7 mol%) (color online)

Fig. 5 displays the calculated bandgap for pure- and Eu^{3+}-doped LiZnVO$_4$, which was about 3.2 eV. This is consistent with the report by Chiu et al., where Eu^{3+}-doped LiZnVO$_4$ was prepared via the sol-gel method [38]. In that work, the authors used the relationship between $(\alpha h v)^2$ and the photon energy hv:

$$\alpha = \frac{C(hv - E_g)^{\frac{1}{2}}}{hv} \qquad (2)$$

where α represents the absorption coefficient, C is a constant, and E_g is the bandgap energy [27]. The calculated Eu^{3+}-doped LiZnVO$_4$ bandgap energy was 3.20–3.22 eV.
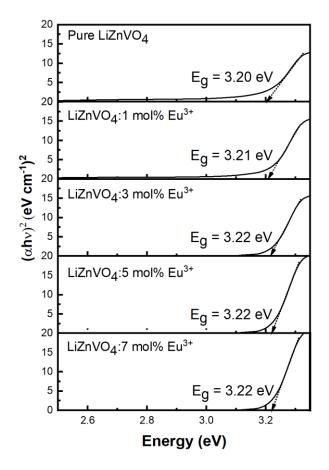

Fig. 5. Bandgap of LiZnVO4:xEu^{3+} (x = 0 mol%, 1 mol%, 3 mol%, 5 mol%, and 7 mol%) annealed at 600ºC.

Figs. 6 (a) and (b) show the excitation and emission spectra of pure LiZnVO$_4$ calcined at 400ºC, 500ºC, 600ºC, and 700ºC. Compared to the other samples, pure LiZnVO$_4$ annealed at 600ºC exhibits a higher emission intensity at 526 nm. The bluish-green light of pure LiZnVO$_4$ is due to the $^3T_1$-$^1A_1$ transition at 526 nm, the main peak [39].
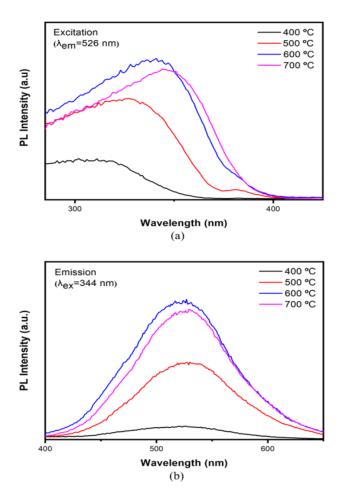

Fig. 6. (a) Excitation and (b) emission spectra of pure LiZnVO4 annealed at 400ºC, 500ºC, 600ºC, and 700℃ for 3 h (color online)

Figs. 7 (a) and (b) present the excitation and emission spectra of LiZnVO$_4$:xEu (x = 0 mol%, 1 mol%, 3 mol%, 5 mol%, and 7 mol%) annealed at 600ºC. The main emission peak decreased as the concentration of Eu^{3+} increased. For the 5 mol% and 7 mol% Eu^{3+}-doped LiZnVO$_4$ samples, the emission peak at 618 nm is due to the $^5D_0 \rightarrow {}^7F_2$ transition that initiated from charge transfer transitions from the VO$_4$$^{3-}$ host to the Eu^{3+} ions [38].
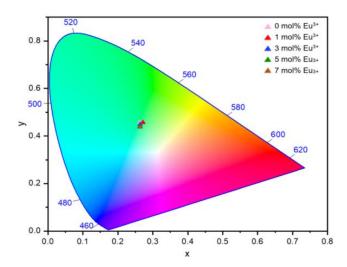
Fig. 7. (a) Excitation and (b) emission spectra of LiZnVO₄:xEu (x = 0 mol%, 1 mol%, 3 mol%, 5 mol%, and 7 mol%) annealed at 600ºC (color online)

The CIE color coordinates of the crystalline LiZnVO₄ doped with different concentrations of Eu^{3+} at $\lambda_{ex} = 344$ nm are shown in Fig. 8. When the amount of Eu^{3+} increased from 0 mol% to 7 mol%, the color coordinates change from x = 0.262 and y = 0.457 (yellow-green) to x = 0.264 and y = 0.437 (blue-green).

The luminescent characteristics of pure and Eu^{3+}-doped LiZnVO₄ were measured (Table 1). Compared with samples obtained by the sol-gel method [41], the characteristics are very similar, except for the crystalline grain size of Eu^{3+}-doped LiZnVO₄, which was larger when using the solid-state method. However, the crystalline grain size of pure LiZnVO₄ remains the largest. Additionally, it is worth noting that the bandgap energy of pure LiZnVO₄ is very similar to that of Eu^{3+}-doped LiZnVO₄.
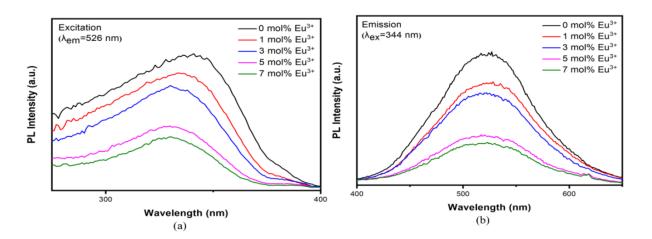

Fig. 8. CIE color coordinate diagram of LiZnVO₄:xEu³⁺ (x = 0 mol%, 1 mol%, 3 mol%, 5 mol%, and 7 mol%) (color online)

4. Conclusion

Eu^{3+}-doped LiZnVO₄ was synthesized via a solid-state reaction. Single rhombohedric LiZnVO₄ crystalline structures were achieved. The crystallinity of the Eu^{3+}-doped LiZnVO₄ particles decreases with increasing Eu^{3+} content. Also, as the concentration of Eu^{3+} increased, the $^7F_0 \rightarrow {}^5D_2$ peak slightly shifted to shorter wavelengths (blue-shift). When comparing the annealing temperatures, the pure LiZnVO₄ sample prepared at 600ºC exhibits a higher emission intensity at 526 nm than the other samples. The absorption bandgap of Eu^{3+}-doped LiZnVO₄ was about 3.20 eV. The CIE emission coordinates of the doped samples change from x = 0.262 and y = 0.457 (yellow-green) to x = 0.264 and y = 0.437 (blue-green) when the Eu^{3+} ions reach 7 mol%.

Table 1. Comparison of pure and Eu^{3+}-doped LiZnVO$_4$ performance.

Composition	Method	Crystalline temperature	Crystalline grain size	CIE color coordinates	A bandgap energy	The extra absorption peak	The emission peak (Wavelength nm)	a dielectric constant (εr)	Reference
LiZnVO₄	Solid-state	600 ℃	59.87 nm	-	3.20 eV		526 nm (λex = 344 nm)		This study
Eu³⁺-doped LiZnVO₄	Solid-state	600 ℃	60.7 nm (1 mol% Eu³⁺)	x = 0.262, y = 0.457	3.21 eV	467 nm and 536 nm	526 nm (λex = 344 nm)		This study
LiZnVO₄	Sol-gol	600 ℃	58 nm	-	3.10 eV	-	529 nm (λex = 325 nm)		[38]
Eu³⁺-doped LiZnVO₄	Sol-gol	600 ℃	73.2 nm (1 mol% Eu³⁺)	x = 0.317, y = 0.423	-	466 nm and 538 nm	529 nm (λex = 325 nm)		[38]
LiZnVO₄	Solid-state	700 ℃	-	-	-	-	560 nm (λex = 340 nm)	7.5	[8]
LiZnVO₄	Sol-gel	600 ℃	-	-	-	-	560 nm (λex = 340 nm)	6.8	[8]
LiZnVO₄	Sol-gel combustion	600 ℃	-	x = 0.31, y = 0.41	-	-	543 nm (λex = 375 nm)		[40]
LiZnVO₄	Combustion	600 ℃	41 nm	-	3.23 eV	-	550 nm (λex = 270 nm)		[41]

References

[1] B. K. Grandhe, S. Ramaprabhu, S. Buddhudu, K. Sivaiah, V. R. Bani, K. Jang, Opt. Commun. **285**, 1194 (2012).

[2] Y. S. Chang, H. J. Lin, Y. L. Chai, Y. C. Li, J. Alloys Compd. **460**, 421 (2008).

[3] I. Gupta, S. Singh, S. Bhagwan, D. Singh, Ceram. Int. **47**, 19282 (2021).

[4] S. K. Gupta, K. Sudarshan, R. M. Kadam, Mater. Today Commun. **27**, 102277 (2021).

[5] T. L. Soundarya, Udayabhanu, Y. T. Ravikiran, B. Nirmala, G. Nagaraju, J. Mater. Sci.: Mater. Electron. **33**, 10902 (2022).

[6] T. Uyama, K. Mukai, Mater. Today Energy **14**, 100331 (2019).

[7] T. L. Soundarya, B. Nirmala, F. A. Alharthi, B. Nagaraj, G. Nagaraju, Mater. Sci. Eng., B **280**, 115718 (2022).

[8] C. Busuioc, S. I. Jinga, J. Optoelectron. Adv. M. **15**(11-12), 1470 (2013).

[9] B. Yan, X.Q. Su, J. Non-Cryst. Solids **352**, 3275 (2006).

[10] T. Uyama, K. Mukai, I. Yamada, Inorg. Chem. **59**, 777 (2020).

[11] T. N. L. Tran, A. Szczurek, S. Varas, C. Armellini, F. Scotognella, A. Chiasera, M. Ferrari, G. C. Righini, A. Lukowiak, Opt. Mater. **124**, 111978 (2022).

[12] C. B. de Araújo, L. R. P. Kassab, D. M. da Silva, Opt. Mater. **131**, 112648 (2022).

[13] Y. Tayal, A. S. Rao, Opt. Mater. **117**, 111112 (2021).

[14] J. Wang, H. Hong, X. Kong, H. Peng, B. Sun, B. Chen, J. Zhang, W. Xu, H. Xia, J. Appl. Phys. **93**, 1482 (2003).

[15] K. B. Kim, K. W. Koo, T. Y Cho, H. G. Chun, Mater. Chem. Phys. **80**, 682 (2003).

[16] Y. Wang, T. Endo, E. Xie, D. He, B. Liu, Microelectron. J. **35**, 357 (2004).

[17] M. H. Huang, T. H. Fang, M. H. Lin, C. W. Chang, Y. C. Fan, Sens. Mater. **32**, 809 (2020).

[18] Z. W. Chiu, Y. J. Hsiao, T. H. Fang, L. W. Ji, Int. J. Electrochem. Sci. **10**, 2391 (2015).

[19] T. H. Fang, Y. S. Chang, L. W. Ji, S. D. Prior, W. Water, K. J. Chen, C. F. Fang, J. Phys. Chem. Solids **70**, 1015 (2009).

[20] Y. J. Hsiao, Y. S. Chang, Y. H. Chang, Mater. Chem. Phys. **100**, 418 (2006).

[21] Z. Wang, D. Yuan, D. Xu, M. Lv, X. Cheng, L. Pan, X. Shi, J. Cryst. Growth **255**, 348 (2003).

[22] L. Tian, B. Y. Yu, C. H. Pyun, H. L. Park, S. I. Mho, Solid State Commun. **129**, 43 (2004).

[23] W. Zhang, Y. Chen, X. Geng, Y. Yang, L. Xiao, J. Lumin. **224**, 117324 (2020).

[24] S. Wang, Y. Xu, T. Chen, W. Jiang, J. Liu, X. Zhang, W. Jiang, L. Wang, Chem. Eng. J. **404**, 125912 (2021).

[25] Y. Zhang, M. Ruan, Q. Zhou, X. Mu, J. Du, E. Xie, Y. Sheng, Z. Zhang, J. Optoelectron. Adv. M. **20**(11-12), 642 (2018).

[26] M. Chang, Y. Song, Y. Sheng, J. Chen, H. Zou, Phys. Chem. Chem. Phys. **19**(26), 17063 (2017).

[27] S. Neeraj, N. Kijima, A. K. Cheetham, Solid State Commun. **131**, 65 (2004).

[28] Y. Lin, F. Xiao, S. Gao, Ionics **19**, 391 (2013).

[29] S. Hua, G. Fu, Sens. Actuators, A **163**, 481 (2010).

[30] G. Fu, H. Chen, Z. Chen, J. Zhang, H. Kohler, Sens.
     Actuators, B **81**, 318 (2002).
[31] S. Hu, H. Chen, G. Fu, F. Meng, Sens. Actuators B
     134, 769 (2008).
[32] G. Fu, H. Chen, S. Hu, Z. Liu, Sens. Actuators B
     137, 17 (2009).
[33] Y. Lee, J. Chae, M. Kang, J. Ind. Eng. Chem. **16**,
     609 (2010).
[34] C. H. Lu, C.T. Chen, J. Sol-Gel Sci. Technol. **43**,
     179 (2007).
[35] R. Wongmaneerung, W. Chaisan, O. Khamman,
     R. Yimnirun, S. Ananta, Ceram. Int. **34**,
     813 (2008).
[36] O. Khamman, R. Wongmaneerung, W. Chaisan,
     R. Yimnirun, S. Ananta, J. Alloys Compd. **456**,
     492 (2008).

[37] M. H. Huang, M. H. Lin, T. H. Fang, C. W. Chang,
     Mater. Res. Express **5**, (2018).
[38] Z. W. Chiu, Y. J. Hsiao, T. H. Fang, L. W. Ji,
     J. Sol-Gel Sci. Technol. **69**, 299 (2014).
[39] Y. J. Hsiao, Y. L. Chai, L. W. Ji, T. H. Fang,
     T. H. Meen, J. K. Tsai, K. L. Chen, S. D. Prior,
     Mater. Lett. **70**, 163 (2012).
[40] N. Pathak, S. K. Gupta, A. Prince, R. M. Kadam,
     V. Natarajan, J. Mol. Struct. **121**, 1056 (2014).
[41] S. Khursheed, V. Kumar, J. Sharma, Mater.
     Focus **5**, 485 (2016).

_____

*Corresponding author: fang@nkust.edu.tw